Deep Super-Resolution of Land Surface Temperature using PlanetScope Imagery and Kolmogorov-Arnold Networks: A Case Study in Germany

Mahdiyeh Fathi [1,2*], Hossein Arefi [1], Reza Shah-Hosseini [2], Armin Moghimi [3]

[1] i3mainz, Institute for Spatial Information and Surveying Technology, Mainz University of Applied Sciences, Mainz, Germany, hossein.arefi@hs-mainz.de,
[2] School of Surveying and Geospatial Engineering, College of Engineering, University of Tehran – Tehran, Iran, mahdiyeh.fathi@ut.ac.ir, rshahosseini@ut.ac.ir
[3] Department of Photogrammetry and Remote Sensing, Geomatics Engineering Faculty, K. N. Toosi University of Technology, Tehran, Iran, moghimi.armin@kntu.ac.ir

KEY WORDS: Planet-Scope, Landsat-8, Drone, LST, Super-Resolution, KANs.

ABSTRACT:
Accurate assessment of the urban heat island (UHI) phenomenon relies on land surface temperature (LST) maps with high spatial-temporal resolution. Although many studies have focused on enhancing the level of spatial detail in LST from MODIS by using Landsat 8 imagery along with advanced deep learning models such as CNNs and GANs, these methods typically require significant computational resources. In addition, the potential of drone-based thermal imagery to enhance the spatial resolution of Landsat 8 insufficiently investigated. In response to these challenges, we present an innovative approach to generate high-resolution LST (LST_{SR}) maps. This approach combines low-resolution Landsat 8 LST data (LST_{LR}) with high-resolution Planet-Scope imagery (I_{HR}) and drone-collected thermal data (T_{HR}) using Kolmogorov-Arnold networks (KAN) augmented by spline-based feature extraction techniques. In this approach, 3-metre Planet-Scope imagery is used to transfer spatial detail to the Landsat-8 LST, while T_{HR} uses as a ground truth data. The LST_{LR} and I_{HR} datasets serve as inputs to the KAN models. We designed and tested KAN architectures: (1) shallow-linear, (2) deep-linear, and (3) deep-nonlinear using training sites in Germany and evaluated their performance at an independent test site. The results showed that the deep-linear model with two hidden layers and five neurons per layer achieved the best performance. This model had an RMSE of 3.65°C, a MAE of 2.70°C, an SSIM of 0.82, a PSNR of 23.13, and a MAPE of 8.33%. It demonstrated a superior ability to capture thermal patterns and reconstruct fine-scale features, such as edges. In contrast, the shallow-linear model performed the worst, with an RMSE of 6.22°C, a MAE of 5.12°C, an SSIM of 0.75, a PSNR of 18.51, and a MAPE of 15.51%.

1. INTRODUCTION

Land Surface Temperature (LST), derived from infrared bands on platforms such as MODIS, Sentinel-3, Landsat 8, and drone systems like the DJI Mavic 3T, plays a vital role in a wide range of applications. These include wildfire detection, forest resource management, hydrological modeling, climate change assessment, precision agriculture, urban heat island (UHI) analysis, urban climate classification using Local Climate Zones (LCZ), and the development of heat-resilient urban environments (Aboutalebi et al., 2022; Asadi et al., 2020; Fathi, Shah-Hosseini, et al., 2025; He et al., 2024; Heidarimozaffar & Arefi, 2023; Malbéteau et al., 2018).

Several techniques have been developed to extract LST from satellite imagery, including single-channel algorithms, split-window methods, and multi-angle approaches (Mathew et al., 2001; Sobrino & Jiménez-Muñoz, 2005). However, in complex environments, particularly urban areas, satellite-derived LST products often fail to capture fine-scale temperature variability caused by heterogeneous surface features. To overcome this limitation, super-resolution (SR) techniques have been proposed to enhance the spatial detail of LST products (Fathi, Shah-Hosseini, et al., 2025; Feng et al., 2015).

SR techniques can generally be categorized into classical and deep learning–based approaches. Classical methods, such as FFT, PCA, and pan-sharpening, offer computational simplicity and efficiency but are often inadequate for resolving high-resolution thermal structures (González-Audícana et al., 2004; Jawak & Luis, 2013; Kumar et al., 2024; Sarp, 2014; Wady et al., 2020). In contrast, modern deep learning frameworks, including GANs, SRCNN, DRCN, ResNet, ResNet-Attention, and ESPCN, produce sharper and more detailed images compared with traditional methods (Chen et al., 2024; Daniels & Bailey, 2023; Fathi, Arefi, et al., 2025; Lloyd et al., 2022; Molliere et al., 2023; Nguyen et al., 2022; Wady et al., 2020). However, implementing these models typically demands substantial computational resources and large training datasets, which can constrain their practicality in real-world scenarios (Fathi, Shah-Hosseini, et al., 2025; Kumar et al., 2024).

Recent research has introduced several advanced architectures aimed at improving the spatial detail of LST and sea surface temperature (SST) imagery. These include cross-scale diffusion networks, attention-based CNNs, SRGANs, STTFNs, VDSR, transformer-based models, and FSRCNN. Such architectures have shown promising results, particularly when applied to MODIS and Landsat 8 data (Chen et al., 2024; Daniels & Bailey, 2023; Haut et al., 2019; Lloyd et al., 2022; Molliere et al., 2023; Nguyen et al., 2022; Passarella et al., 2022; Yin et al., 2021; Zou et al., 2023).

Despite their global coverage, satellite-derived LST measurements are constrained by environmental factors such as atmospheric variability, differences in surface emissivity, and complex terrain characteristics. Drone-based thermal imagery provides high spatial precision but is limited in spatial coverage. Similarly, while deep learning models yield high accuracy, their reliance on powerful computational infrastructure and extensive training data can hinder widespread adoption (Fathi, Shah-Hosseini, et al., 2025; Sattari & Hashim, 2014; Science, n.d.). Therefore, there is a pressing need for efficient and cost-effective approaches capable of producing

* Corresponding author

This contribution has been peer-reviewed. The double-blind peer-review was conducted on the basis of the full paper.
https://doi.org/10.5194/isprs-annals-X-4-W8-2025-243-2026 | © Author(s) 2026. CC BY 4.0 License.

high-resolution LST maps without demanding significant computational resources.

To address this challenge, we propose a novel method that employs Kolmogorov–Arnold Networks (KANs) to fuse multi-source data, including Landsat 8 LST, PlanetScope imagery, and high-resolution drone-based thermal data, to generate 3-meter LST maps. KANs efficiently capture complex spatial patterns with low computational cost by combining spline functions with multilayer perceptrons (Addas et al., 2020; Fathi, Shah-Hosseini, et al., 2025; Liu et al., 2024). Our proposed framework enhances spatial detail and supports applications in urban studies, precision agriculture, and local climate monitoring.

2. MATERIAL

2.1 Study area

This study focuses on three villages in Germany: Oberfischbach and Mittelfischbach, located in the state of Rhineland-Palatinate, which were selected as training sites, and Königshain, located in the state of Saxony, which was chosen as the test site to evaluate the model's performance. A visual overview of the study area is shown in Figure 1.

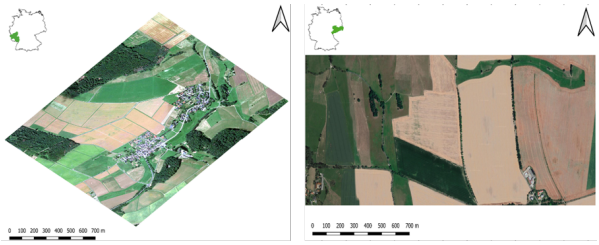

(a) (b)

Figure 1. Study area. (a) Training sites: Oberfischbach and Mittelfischbach (Rhineland-Palatinate); (b) Test site: Königshain (Saxony).

2.2 Datasets

In this study, data were obtained from three primary sources: high-resolution thermal imagery (TH_{HR}) acquired using the DJI Mavic 3T (DJI M3T) drone (Table 1), low-resolution Landsat 8 land surface temperature (LST_{LR}), and high-resolution PlanetScope imagery (I_{HR}). All datasets were acquired between July and September 2024 (Table 2).

Item	Camera configuration
DJI M3T	Camera configuration Weight: 920 g Max. Flight Time: 45 min Max. Speed: 21 m/s Operating Temperature: -10 to 40 °C
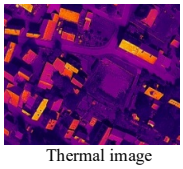 Thermal image	Thermal camera Resolution: 640 × 512 pixels Spectral Range: 8 – 14 µm Accuracy: ±2 °C Field of View (FOV): 61° Focal Length: 40mm

Table 1. Specifications of the DJI Mavic 3T (Fathi, Arefi et al. 2025, https://www.hammermissions.com/post/dji-mavic-3t-cameras-explained).

Drone and Landsat 8	PlanetScop	Site
2024/07/29	2024/07/29	Oberfischbach
2024/08/17	2024/08/14	Konigshain
2024/09/07	2024/09/07	Oberfischbach
2024/09/07	2024/09/07	Mittelfischbach

Table 2. Dates of data acquisition for all datasets used in this study.

3. METHODOLOGY

In this study, a novel super-resolution (SR) framework is proposed to enhance the spatial resolution of land surface temperature (LST) derived from Landsat 8 imagery. The proposed method integrates high-resolution imagery (I_{HR}) with a Kolmogorov–Arnold Network (KAN), as illustrated in the flowchart presented in Figure 2.

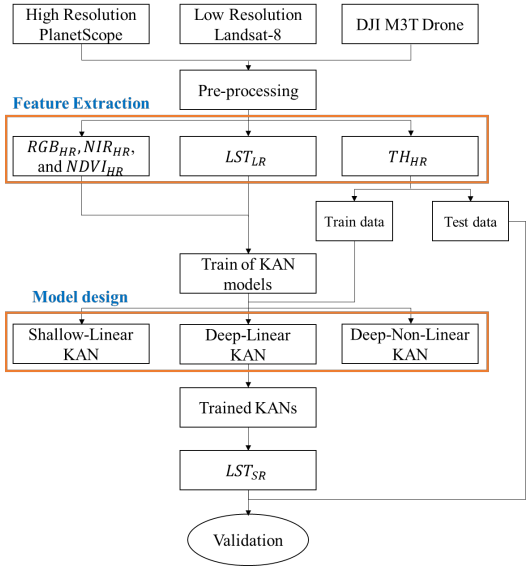

Figure 2. Flowchart of the proposed super-resolution (SR) method.

3.1 Pro-Processing and Feature Extraction

In this step, several features, including the Red_{HR}, $Green_{HR}$, $Blue_{HR}$, and NIR_{HR} bands, as well as $NDVI_{HR}$from I_{HR} and LST_{LR}, are collected as inputs to the model. The LST_{LR} is calculated using the Planck algorithm (Zahrotunisa, 2022). These features provide essential spectral and thermal information about the land surface.

Second, the thermal images captured by the DJI M3T drone do not directly provide absolute temperature values. The DJI Thermal SDK is used to convert the raw thermal data into absolute temperature (https://github.com/DanGeosptial/dji_m3t_rpeg_to_tif, and

https://www.dji.com/downloads/softwares/dji-thermal-sdk).
This script calibrates the raw data and converts it to absolute temperature by incorporating parameters such as emissivity, humidity, camera-to-target distance, and surface reflectance. After conversion, thermal ortho-images are generated using Agisoft Metashape software.
Third, all datasets are spatially co-registered and resampled to a uniform resolution of 3 m to ensure spatial alignment and consistency. Fourth, T_{HR} observations obtained from the DJI M3T drone are used as ground-truth data. Next, the datasets are divided into training and testing subsets to evaluate various KAN architectures, including shallow-linear, deep-linear, and deep-nonlinear configurations. Finally, the KAN model that achieves the highest accuracy in reconstructing LST_{SR} is selected as the optimal configuration.

3.2 Model Design and implementation

In this step, the various KAN models implemented to investigate the reconstruction of LST_{SR} are described. Kolmogorov–Arnold Networks (KANs) are dynamic, fully connected, and interpretable architectures based on the Cauchy–Kolmogorov theorem (Liu et al., 2024). According to this theorem, a continuous multivariate function $f(x_1,\ldots,x_n)$ can be decomposed into a composition of univariate functions $\varphi(x)$, either in the form of a weighted linear sum or a nonlinear weighted product, as expressed in Equations (1) and (2) (Fathi, Shah-Hosseini, et al., 2025).

$$x=[x_1,\ldots,x_n] \quad (1)$$

$$h_i=\sum_{(i=1:n)} \emptyset_{i,j}(x_i)+\sum_{(i\neq k)} \emptyset_{i,j}(x_i).\emptyset_{k,j}(x_k) \quad (2)$$

Unlike multi-layer perceptrons (MLPs), which combine inputs through fixed linear operations, KANs employ learnable spline functions for composition. This mechanism eliminates the dependence on fixed weights and enhances representational accuracy, particularly at boundaries and edges (Liu et al., 2024). KANs support flexible architectural depth, ranging from shallow to deep configurations. Due to their unique design, they can achieve high accuracy without requiring deeper networks or an increased number of parameters, often outperforming conventional models under comparable conditions. Figure 3 illustrates four KAN architectures with different depths and levels of nonlinearity (Liu et al., 2024; https://github.com/team-daniel/KAN/tree/master).

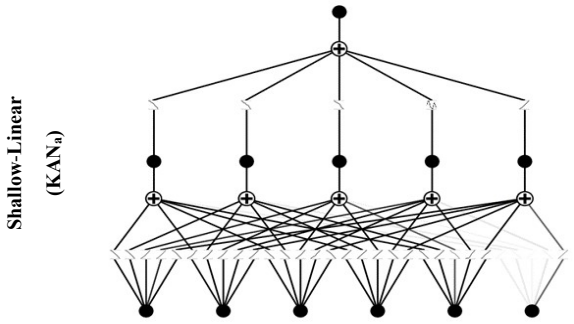

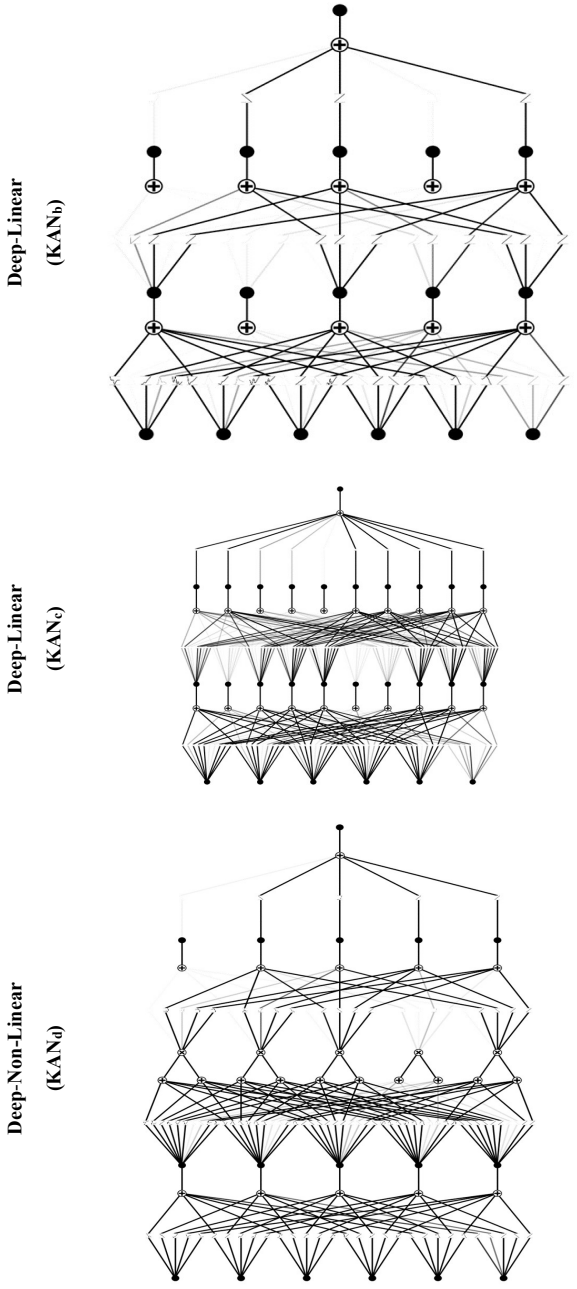

Figure. 3. The four KAN architectures used in this study.

KAN_a is a shallow-linear network consisting of a single hidden layer with five neurons.
KAN_b is a deep-linear architecture comprising two hidden layers, each containing five neurons.
KAN_c is a deep-linear model with two hidden layers, each containing ten neurons.
In contrast, KAN_d is a deep-nonlinear architecture with two hidden layers, each containing five neurons.
All models were trained using the Adam optimizer with a learning rate of 0.05, a batch size of 50, and 100 epochs. The Mean Squared Error (MSE) was employed as the loss function. The dataset was divided into 229,729 training pixels, 98,456 validation pixels, and 190,554 test pixels (Fathi, Shah-Hosseini, et al., 2025). Model performance was evaluated using multiple

quantitative metrics, including RMSE, MAE, MAPE, PSNR, SSIM, and R^2 (Fathi, Shah-Hosseini, et al., 2025).

4. RESULT

The performance of the four KAN architectures was compared to assess their ability to enhance the spatial detail of LST_{LR}. The results of this comparison, based on several evaluation metrics, are summarized in Table 3.

Model	RMSE (°C)	MAE (°C)	MAPE (%)	PSNR	SSIM	R^2
KAN_a	6.22	5.12	15.51	18.51	0.75	-0.50
KAN_b	3.65	2.70	8.33	23.13	0.82	0.48
KAN_c	4.80	4.05	12.89	20.75	0.79	0.10
KAN_d	4.65	3.90	12.33	21.03	0.73	0.16

Table 3. Comparison of KAN model performance for LST_{SR} reconstruction at the test site.

Among the evaluated models, KAN_a exhibited the lowest performance, with an RMSE of 6.22 °C. In contrast, KAN_b achieved the best results, reducing the RMSE to 3.65 °C, representing a 41.3% improvement relative to KAN_a. Similarly, the MAE decreased from 5.12 °C to 2.70 °C, an improvement of approximately 47.3%.

KAN_a recorded the highest MAPE (15.51%), indicating poor reconstruction accuracy. Conversely, KAN_b substantially improved this metric, reducing the MAPE to 8.33%, a 46.3% enhancement. Regarding image quality, KAN_b achieved a PSNR of 23.13 compared to 18.51 for KAN_a (a 24.9% increase). The SSIM also improved from 0.75 to 0.82 (9.3% increase). Markedly, the R^2 exhibited the most significant change, increasing from −0.50 to 0.48, reflecting a noticeable improvement in model accuracy.

KAN_c demonstrated moderate performance. Its RMSE (4.80 °C) was 22.3% lower than KAN_a but 31.5% higher than KAN_b. Although its MAPE (12.89%) was lower than KAN_a, it remained 54.7% higher than KAN_b. The SSIM of 0.79 was close to KAN_b's 0.82, indicating reasonable structural preservation. Its R^2 value (0.10) showed slight improvement over KAN_a, but overall reconstruction performance remained weak.

KAN_d outperformed KAN_a across most metrics but did not reach the accuracy of KAN_b. Its RMSE (4.65 °C) was 25.2% lower than KAN_a but 27.4% higher than KAN_b. The MAPE (12.33%) represented a 20.5% improvement over KAN_a, but remained 48% worse than KAN_b. Its PSNR (21.03) was 13.6% higher than KAN_a but 9.1% lower than KAN_b. The SSIM value (0.73) was the second lowest among all models, while the R^2 value (0.16) indicated some improvement but still modest accuracy overall.

Figure 4 presents the super-resolved (SR) LST_{LR} maps generated by the four KAN architectures. Among these, KAN_b and KAN_d produced outputs most visually consistent with TH_{HR}, demonstrating more accurate reconstruction of fine-scale spatial details compared with the original LST_{LR} maps. These findings confirm that KAN-based networks are effective in enhancing spatial resolution in thermal imagery.

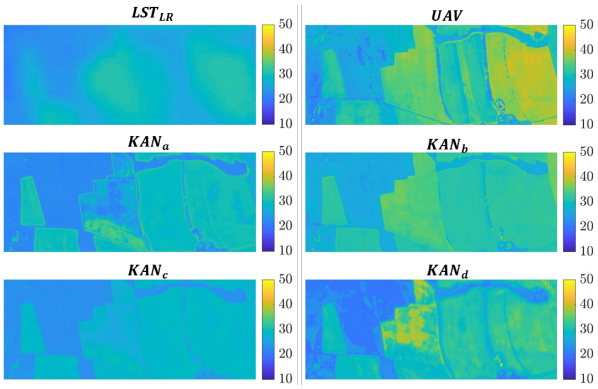

Figure. 4. Comparison of generated LST_{SR} maps using KANs.

The histograms presented in Fig. 5 illustrate the temperature distribution of four different KAN models in comparison with TH_{HR} and LST_{LR}.

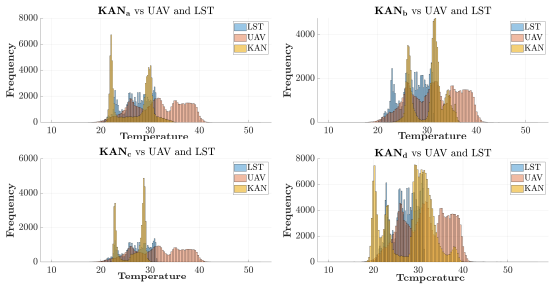

Figure. 5. Comparison of LST_{SR} histogram distributions produced by the four KAN models.

In KAN_a, the LST_{SR} distribution is clearly separated from both LST_{LR} and drone-based (TH_{HR}) data, with mismatched peaks and temperature ranges, resulting in a negative R^2 and reduced model accuracy. In contrast, KAN_b exhibits substantial overlap with both LST_{LR} and TH_{HR}, showing nearly identical peaks and ranges, consistent with its superior quantitative performance. KAN_c demonstrates moderate overlap, though discrepancies in peak density remain. Finally, KAN_d also shows good alignment, with a slightly broader temperature range than the reference data, but its performance remains below that of KAN_b.

5. CONCLUSIONS

This study evaluated four KAN architectures to enhance the spatial resolution of LST derived from Landsat 8 imagery using PlanetScope optical remote sensing data. Among the configurations tested, the deep-linear model, with two hidden layers, each containing five neurons, achieved the best performance, outperforming both the shallow-linear and deep-nonlinear architectures. It attained a PSNR of 23.13 and a SSIM of 0.82 at the test site. Furthermore, it yielded an R^2 value of 0.48, demonstrating a strong capability to extract spatial details and edge features from PlanetScope imagery and effectively integrate them into the LST_{LR} maps.

Overall, the results underscore the effectiveness of the KAN framework in enhancing the spatial detail of LST_{LR} products and highlight its potential for advanced applications in thermal remote sensing, urban climate studies, and precision environmental monitoring.

ACKNOWLEDGEMENTS

We sincerely thank Sven Kaulfersch (sven.kaulfersch@hs-mainz.de) for his valuable support in acquiring drone data. His assistance was instrumental in the data collection process, and we deeply appreciate his contributions to this study.

REFERENCES

Aboutalebi, M., Torres-Rua, A. F., McKee, M., Kustas, W. P., Nieto, H., Alsina, M. M., White, A., Prueger, J. H., McKee, L., Alfieri, J., Hipps, L., Coopmans, C., Sanchez, L., Dokoozlian, N., 2022. Downscaling UAV land surface temperature using a coupled wavelet-machine learning-optimization algorithm and its impact on evapotranspiration. Irrigation Science, 40(4–5), 553–574. https://doi.org/10.1007/s00271-022-00801-2

Addas, A., Goldblatt, R., Rubinyi, S., 2020. Utilizing remotely sensed observations to estimate the urban heat Island effect at a local scale: Case study of a University campus. Land, 9(6). https://doi.org/10.3390/LAND9060191

Asadi, A., Arefi, H., Fathipoor, H., 2020. Simulation of green roofs and their potential mitigating effects on the urban heat island using an artificial neural network: A case study in Austin, Texas. Advances in Space Research, 66(8). https://doi.org/10.1016/j.asr.2020.06.039

Chen, J., Jia, L., Zhang, J., Feng, Y., Zhao, X., Tao, R., 2024. Super-Resolution for Land Surface Temperature Retrieval Images via Cross-Scale Diffusion Model Using Reference Images. Remote Sensing, 16(8), 1–24. https://doi.org/10.3390/rs16081356

Daniels, J., Bailey, C. P., 2023. Reconstruction and Super-Resolution of Land Surface Temperature Using an Attention-Enhanced CNN Architecture. International Geoscience and Remote Sensing Symposium (IGARSS), 2023-July, 4863–4866. https://doi.org/10.1109/IGARSS52108.2023.10281446

Fathi, M., Arefi, H., Shah-Hosseini, R., Moghimi, A., 2025. Super-Resolution of Landsat-8 Land Surface Temperature Using Kolmogorov–Arnold Networks with PlanetScope Imagery and UAV Thermal Data. Remote Sensing, 17(8). https://doi.org/10.3390/rs17081410

Fathi, M., Shah-Hosseini, R., Moghimi, A., Arefi, H., 2025. MHRA-MS-3D-ResNet-BiLSTM: A Multi-Head-Residual Attention-Based Multi-Stream Deep Learning Model for Soybean Yield Prediction in the U.S. Using Multi-Source Remote Sensing Data. Remote Sensing, 17(1). https://doi.org/10.3390/rs17010107

Feng, X., Foody, G., Aplin, P., Gosling, S. N., 2015. Enhancing the spatial resolution of satellite-derived land surface temperature mapping for urban areas. Sustainable Cities and Society, 19. https://doi.org/10.1016/j.scs.2015.04.007

González-Audícana, M., Saleta, J. L., Catalán, R. G., García, R., 2004. Fusion of multispectral and panchromatic images using improved IHS and PCA mergers based on wavelet decomposition. IEEE Transactions on Geoscience and Remote Sensing, 42(6). https://doi.org/10.1109/TGRS.2004.825593

Haut, J. M., Paoletti, M. E., Fernandez-Beltran, R., Plaza, J., Plaza, A., Li, J., 2019. Remote sensing single-image superresolution based on a deep compendium model. IEEE Geoscience and Remote Sensing Letters, 16(9). https://doi.org/10.1109/LGRS.2019.2899576

He, B. J., Fu, X., Zhao, Z., Chen, P., Sharifi, A., Li, H., 2024. Capability of LCZ scheme to differentiate urban thermal environments in five megacities of China: Implications for integrating LCZ system into heat-resilient planning and design. IEEE Journal of Selected Topics in Applied Earth Observations and Remote Sensing, 17, 18800–18817. https://doi.org/10.1109/JSTARS.2024.3469241

Heidarimozaffar, R. G. M., Arefi, A. S. H., 2023. Land surface temperature analysis in densely populated zones from the perspective of spectral indices and urban morphology. International Journal of Environmental Science and Technology, 20(3), 2883–2902. https://doi.org/10.1007/s13762-022-04725-4

Jawak, S. D., Luis, A. J., 2013. A Comprehensive Evaluation of PAN-Sharpening Algorithms Coupled with Resampling Methods for Image Synthesis of Very High Resolution Remotely Sensed Satellite Data. Advances in Remote Sensing, 02(04). https://doi.org/10.4236/ars.2013.24036

Kumar, D. L., Rajaan, R., Choudhary, D. N., Sharma, D. A., 2024. A Comprehensive Review and Comparison of Image Super-resolution Techniques. International Journal of Advanced Engineering, Management and Science, 10(2), 40–45. https://doi.org/10.22161/ijaems.102.5

Liu, Z., Wang, Y., Vaidya, S., Ruehle, F., Halverson, J., Soljačić, M., Hou, T. Y., Tegmark, M., 2024. KAN: Kolmogorov-Arnold Networks. 1–50. http://arxiv.org/abs/2404.19756

Lloyd, D. T., Abela, A., Farrugia, R. A., Galea, A., Valentino, G., 2022. Optically Enhanced Super-Resolution of Sea Surface Temperature Using Deep Learning. IEEE Transactions on Geoscience and Remote Sensing, 60, 1–14. https://doi.org/10.1109/TGRS.2021.3094117

Malbéteau, Y., Parkes, S., Aragon, B., Rosas, J., McCabe, M. F., 2018. Capturing the diurnal cycle of land surface temperature using an unmanned aerial vehicle. Remote Sensing, 10(9). https://doi.org/10.3390/rs10091407

Mathew, K., Nagarani, C. M., Kirankumar, A. S., 2001. Split-window and multi-angle methods of sea surface temperature determination: An analysis. International Journal of Remote Sensing, 22(16). https://doi.org/10.1080/01431160152558341

Molliere, C., Gottfriedsen, J., Langer, M., Massaro, P., Soraruf, C., Schubert, M., 2023. Multi-Spectral Super-Resolution of Thermal Infrared Data Products for Urban Heat Applications. International Geoscience and Remote Sensing Symposium (IGARSS), 2023-July, 4919–4922. https://doi.org/10.1109/IGARSS52108.2023.10283339

Nguyen, B. M., Tian, G., Vo, M. T., Michel, A., Corpetti, T., Granero-Belinchon, C., 2022. Convolutional Neural Network Modelling for MODIS Land Surface Temperature Super-Resolution. European Signal Processing Conference, 2022-Augus, 1806–1810. https://doi.org/10.23919/eusipco55093.2022.9909569

Passarella, L. S., Mahajan, S., Pal, A., Norman, M. R., 2022. Reconstructing High Resolution ESM Data Through a Novel Fast Super Resolution Convolutional Neural Network (FSRCNN). Geophysical Research Letters, 49(4). https://doi.org/10.1029/2021GL097571

Sarp, G., 2014. Spectral and spatial quality analysis of pan-sharpening algorithms: A case study in Istanbul. European Journal of Remote Sensing, 47(1). https://doi.org/10.5721/EuJRS20144702

Sattari, F., Hashim, M., 2014. A Breif Review of Land Surface Temperature Retrieval Methods from Thermal Satellite Sensors. Middle-East Journal of Scientific Research, 22(5).

Science, E. (n.d.). Correlation analysis of Land Surface Temperature (LST) measurement using DJI Mavic Enterprise Dual Thermal and Landsat 8 Satellite Imagery (case study : Surabaya City) Correlation analysis of Land Surface Temperature (LST) measurement using DJI Mavi. https://doi.org/10.1088/1755-1315/936/1/012037

Sobrino, J. A., Jiménez-Muñoz, J. C., 2005. Land surface temperature retrieval from thermal infrared data: An assessment in the context of the Surface Processes and Ecosystem Changes Through Response Analysis (SPECTRA) mission. Journal of Geophysical Research D: Atmospheres, 110(16). https://doi.org/10.1029/2004JD005588

Wady, S. M. A., Bentoutou, Y., Bengermikh, A., Bounoua, A., Taleb, N., 2020. A new IHS and wavelet based pansharpening algorithm for high spatial resolution satellite imagery. Advances in Space Research, 66(7). https://doi.org/10.1016/j.asr.2020.06.001

Yin, Z., Wu, P., Foody, G. M., Wu, Y., Liu, Z., Du, Y., Ling, F., 2021. Spatiotemporal Fusion of Land Surface Temperature Based on a Convolutional Neural Network. IEEE Transactions on Geoscience and Remote Sensing, 59(2), 1808–1822. https://doi.org/10.1109/TGRS.2020.2999943

Zahrotunisa, S., 2022. Comparison of Split Windows Algorithm and Planck Methods for Surface Temperature Estimation Based on Remote Sensing Data in Semarang. 14(1), 11–21.

Zou, R., Wei, L., Guan, L., 2023. Super Resolution of Satellite-Derived Sea Surface Temperature Using a Transformer-Based Model. Remote Sensing, 15(22). https://doi.org/10.3390/rs15225376